JOURNAL OF Applied Polymer SCIENCE

Description of second flow field via the deformation of polystyrene phase in high-density polyethylene matrix

Quan-Ping Zhang,[1] Xiao-Chao Xia,[2] Shan He,[2] Jian-Min Feng,[2] Ming-Bo Yang,[2] Yin-Tao Li,[1] Yuan-Lin Zhou[1]

[1]State Key Laboratory Cultivation Base for Nonmetal Composites and Functional Materials, Southwest University of Science and Technology, Mianyang 621010, People's Republic of China

[2]College of Polymer Science and Engineering, State Key Laboratory of Polymer Materials Engineering, Sichuan University, Chengdu 610065, People's Republic of China

Correspondence to: M.-B. Yang (E-mail: yangmb@scu.edu) and Q.-P. Zhang (E-mail: zhangqp@swust.edu.cn)

ABSTRACT: Real flow field has been critical in all kinds of injection molding, not only for understanding morphological evolution, but also for tailoring polymer physical property. Since the relaxation of PS phase in the HDPE matrix is successfully retarded by introduction of additional gas cooling, here, the second flow field in gas-assisted injection molding is first calculated with the classical models for predicting the shapes of dispersed droplets in immiscible blend. The results indicate high gas penetration pressure facilitates strong second flow field. Gas penetration time is inversely proportional to the triggered flow intensity, which can be used for the qualitative comparison of the flow fields under various conditions. Importantly, the flow field can be designed by tailoring melt advancing rate, such as the penetration power and/or the penetration resistance of second fluid, which contributes to realizing the optimum coupling between external fields and chain architectures. Besides, this work opens a window for the understanding of real flow field under various processing conditions. © 2016 Wiley Periodicals, Inc. J. Appl. Polym. Sci. **2016**, *133*, 43374.

KEYWORDS: blends; morphology; phase behavior; structure–property relations

Received 10 September 2015; accepted 22 December 2015
DOI: 10.1002/app.43374

INTRODUCTION

The "structuring" processing for polymers has attracted extensive attention in the academic community, which is proposed to tune hierarchical structures under various molding technologies.[1] By describing the external fields, such as flow field[2–4] and temperature gradient,[5,6] or *in situ* monitoring the morphological evolution[7,8] during molding processes, the roles of processing parameters, such as temperature and flow rate,[9,10] on the hierarchical structures of polymers can be tuned. One of the hot topics under injection molding is the variety of descriptions of the real flow fields because of their significant potential applications. For example, quantitative tailoring shear gradients have lent a strong impetus to design polymer morphologies, including crystalline polymorphism,[10–12] orientation[10–13] and phase separation behavior,[14] and so on.

In parallel to the intensive studies on the real flow fields in conventional injection moldings (CIM),[2–4] understanding the complex flow fields in injection molding technologies with a second fluid injection, such as gas-assisted injection molding (GAIM),[15,16] water-assisted injection molding (WAIM)[17,18] and multimelt multi-injection molding (MMMIM)[19,20] has also been of great interest in that it promotes the "structuring" processing of polymers. Their main feature can be summarized as below. First, mold cavity is partially filled with a first melt, that is, short shot or first shot. Then a second fluid (gas, liquid, or melt, for example) penetrates and propels the first melt forward until the cavity is occupied entirely, as shown in Figure 1(a). The polymer melt in the conditions is confined by both the mold wall and the second fluid injection, and exposed to successive intense flows that include the short shot and the second fluid penetrating the first melt, involving multiphase multiflows. Moreover, complex interactions regarding stress and heat transfer between the mold, the melt and the second fluid also tend to occur during the molding process. Therefore, due to the great complexity, frequently used methods for CIM process, either numerical simulation[2–7] (e.g., Moldflow analysis software) or *in situ* monitoring,[8,9] is difficult to accurately reflect the real flow fields.

Additional Supporting Information may be found in the online version of this article.

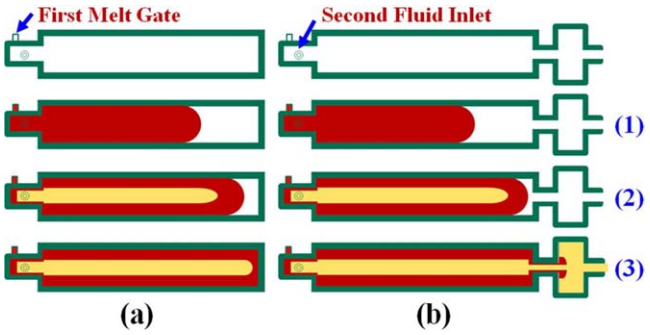

Figure 1. Diagram of the injection molding process with a second fluid injection, (1) melt short shot; (2) second fluid injection; (3) packing and cooling. [Color figure can be viewed in the online issue, which is available at wileyonlinelibrary.com.]

To achieve an accurate but simple description for the complex flow field, other measures should be explored. Here, a series of classical models for predicting the shapes of dispersed droplets in immiscible blend are considered.[21–26] The capillary number:

$$C_a = \frac{\eta_m R\dot{\gamma}}{\sigma}, \quad (1)$$

represents the ratio between flow field (with η_m the viscosity of matrix phase and $\dot{\gamma}$ the local shear rate), and interfacial stress (with σ the interfacial tension and R the radius of dispersed phase). At a given blend, a critical value of the capillary number, $C_{a\ crit}$, is existed and the droplets deformation is an increasing function of C_a. When C_a reaches $C_{a\ crit}$, no steady droplet shape is possible anymore and the droplets irreversibly deform and until break up. Under such conditions, the droplets tend to deform in an "affine" manner. Different affine models are utilized under different conditions, which depend on the viscosity ratio and the capillary number. For viscosity ratio about 1, C_a less than 10 generates cylinder or spheroid model under large strain, while ellipsoidal model generates under much larger C_a,[21,24] such as the intense flow under injection molding. Here, a classical ellipsoidal model has been proposed to describe the intense flow on droplet shapes[21,25,26]:

$$\frac{L}{2R} = \sqrt{1+\frac{\gamma^2}{2}+\frac{\gamma}{2}\sqrt{\gamma^2+4}}, \quad (2)$$

$$\frac{B}{2R} = \left(\frac{L}{2R}\right)^{-1}, \quad (3)$$

$$\gamma = \dot{\gamma}t, \quad (4)$$

where L, R, B, γ, $\dot{\gamma}$, and t is the length of ellipsoidal droplets, the radius of original droplets, the diameter of ellipsoidal droplets, the shear strain, the shear rate, and the shear duration, respectively. Combined with eqs. (1–4), the deformation behaviors of dispersed droplets in blend can be overall depicted from weak to strong shear.

Based on the classical models, the shear imposed on a blend should be reversely calculated with eqs. (1–4), if the relaxation of dispersed phase can be controlled effectively. Unfortunately, the relaxation is unavoidable because of the higher temperature field in the inner zone of molded parts during most of molding processes. For this reason, little work concerning the description of flow field via the deformation of dispersed phase has been reported, especially for the complex conditions with multiphase multiflows.

In this work, the tough problem has been tactfully overcome by tailoring fluid flow pattern during GAIM process, as displayed in Figure 1(b). Compared with previous molding process,[16,27] high-pressure gas is able to discharge outside instead of stay in gas channel, which can additionally promote the cooling of molded parts by convective heat transfer from the gas channel to outside. Then gas injection stage is consisted of gas penetration, gas cooling, and packing stages instead of gas penetration and gas packing stages. The gas injection plays two major roles in molded parts. It penetrates and pushes the first melt forward, meanwhile triggers an intense second flow field, which induces polymer chains to orient and dispersed phase to deform.[16,27–29] Particularly, the cooling of molded parts is rapidly increased,[30,31] which contributes to retaining the shapes of dispersed phase instead of great relaxation, especially for gas channel zone (Figure S1, Supporting Information).

Herein, the second flow field triggered by the second gas penetrating the first melt has been described via the deformation of dispersed phase. The high-density polyethylene/polystyrene (HDPE/PS, 80/20) is selected because both polymers are effective extrusion grade materials and are severe incompatible blend systems that contribute to telling the PS phase apart from the HDPE matrix. What is more, due to the amply high cooling rate, the relaxation of PS phase can be effectively retarded in GAIM parts. As a result, the requirements of calculation for the intensity of flow field with the classical models are achieved.

EXPERIMENTAL

Materials

A commercially available HDPE (5000S), with a melt flow rate (MFR) of 2.1 g/10 min (190°C, 2.16 kg, ASTM D1238-10) and a weight-average molecular weight (M_w) = 3.16 × 10^5 g/mol, was supplied by Lanzhou Petrochemical Corp., Gansu Province, China. The polystyrene (PS, GP5250) with a melt flow rate (MFR) of 7.0 g/mol (200°C, 5 kg, ASTM D1238-10), a M_w of 2.33 × 10^5 g/mol and a density of 1.04–1.06 g/cm^{3,} was obtained from Taihua Plastic (Ningbo), Zhejiang Province, China.

Samples Preparation

In order to obtain distinct phase morphology, the system of HDPE/PS (80/20) was selected. The mixture with HDPE/PS was first melt blended in a TSSJ-25 twin-screw extruder to produce pellets. Then, the pellets were fully dried for the following injection molding. The screw speed was fixed at 45 rpm, and the melt temperature was limited within 190–220°C from hopper to die.

A PS40E5ASE injection molding machine and a MPC-01 gas pressure controller (Zhongtuo, Beijing, China) were used for the molding of GAIM parts. To highlight the second flow field on the deformation of PS phase, the injection rate of first melt was set as slow as possible. The fixed gas penetration time was set as 1 s, which was sure to fulfill the gas penetration. The gas injection without delaying time avoided the relaxation behavior

Table I. Key Parameters Applied in the Molding Processes

Operational variables	Short shot parts	GAIM parts
Melt temperature (°C)	220	220
Mold temperature (°C)	60	60
Shot size (%)	78	78
Injection speed (cm^3/s)	16.5	16.5
Injection pressure (MPa)	100	100
Gas delay time (s)	-	0
Gas penetration pressure (MPa)	-	6.2, 8.3, 10.4
Gas penetration time (s)	-	1
Gas packing and cooling pressure (MPa)	-	10.4
Gas packing and cooling time (s)	-	20
Gas temperature (°C)	-	10.0

of the PS phase during the time. The detailed parameters of GAIM process are listed in Table I. It is noted that the mold with a circular cross-section cavity was employed to afford an even route for gas penetration. Second, a subcavity was designed to connect to the main cavity and outside by two narrow flow channels, as displayed in Figure 1(b), which was different from our previous mold.[16] With this new design, not only a stronger and well-distributed flow field triggered by the second gas penetrating the first melt was guaranteed, but also the cooling rate of molded parts was additionally promoted by gas convective heat transferring from the gas channel to outside.[30–32] The length and parts thickness of the hollow GAIM parts were 180.0 mm and about 1.5 mm, respectively.

To show the second flow field caused by gas penetrating melt on the deformation of PS phase in GAIM parts, the short shot parts were also molded by GAIM technology but without gas injection. The parameters are also listed in Table I. The length

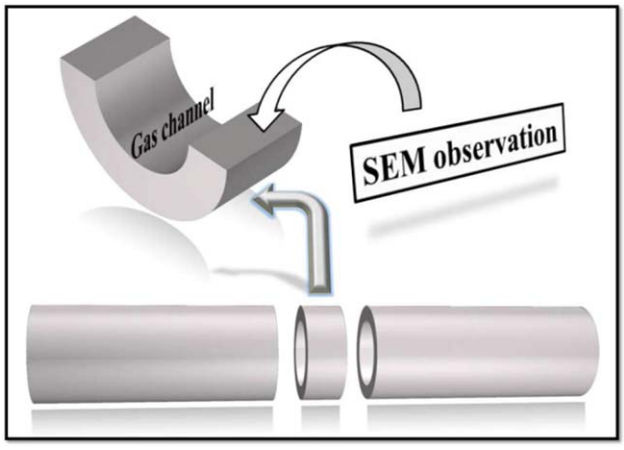

Figure 2. Diagram of morphology observation for the GAIM parts. [Color figure can be viewed in the online issue, which is available at wileyonlinelibrary.com.]

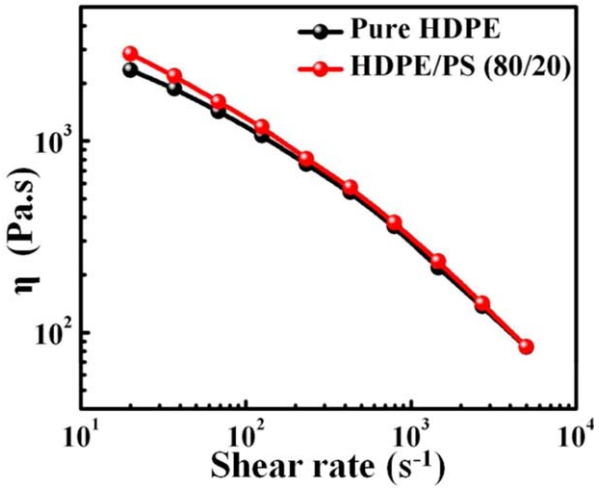

Figure 3. Apparent viscosities of the pure HDPE and the blend. [Color figure can be viewed in the online issue, which is available at wileyonlinelibrary.com.]

and diameters of the solid short shot parts were 100.0 and 8.0 mm, respectively.

Shear Viscosity of Polymer Melt

The apparent shear viscosity of the HDPE and the blend of HDPE/PS were performed on a Rosand RH7D capillary viscosity. The testing temperature was fixed at 220°C (injection molding temperature) and the shear rate range was from 50 to 5000 s^{-1}, which was designed to figure out whether the rheological behavior of the blend can be utilized for representing that of the neat HDPE under an injection molding condition with intense flows.

Scanning Electron Microscope (SEM) and Image Analysis

The test samples were first cut into a segment of 5.0 mm in length about 70 mm from the first melt gate for the GAIM parts, as shown in Figure 2, and cryogenically fractured in liquid nitrogen, then etched by dimethylbenzene at 25°C for 6 h to remove the PS droplets that avoids the confusion between HDPE matrix and PS phase. Furthermore, the fractured surfaces were covered with a thin layer of gold and observed by a JSM-5900LV SEM instrument operating at 20 kV. Finally, PS traces or cavities in molded parts were measured during the SEM observation. The average values were taken as the average diameters of PS phase. The cut position, sample treatment, SEM observation and data analysis for the short shot parts were the same as that of the GAIM parts.

RESULTS AND DISCUSSION

Apparent Viscosity

To verify whether the HDPE and the blend show consistency in rheological behaviors under intense flows, the apparent viscosities of the polymers are surveyed over a wide range of shear rates. As depicted in Figure 3, the selected blend has a slightly higher viscosity than the HDPE in the low shear rates. Along with the increase in shear rates, the viscosity differences between the HDPE and the blend become negligible, which contribute to the distribution of PS phase in the HDPE matrix

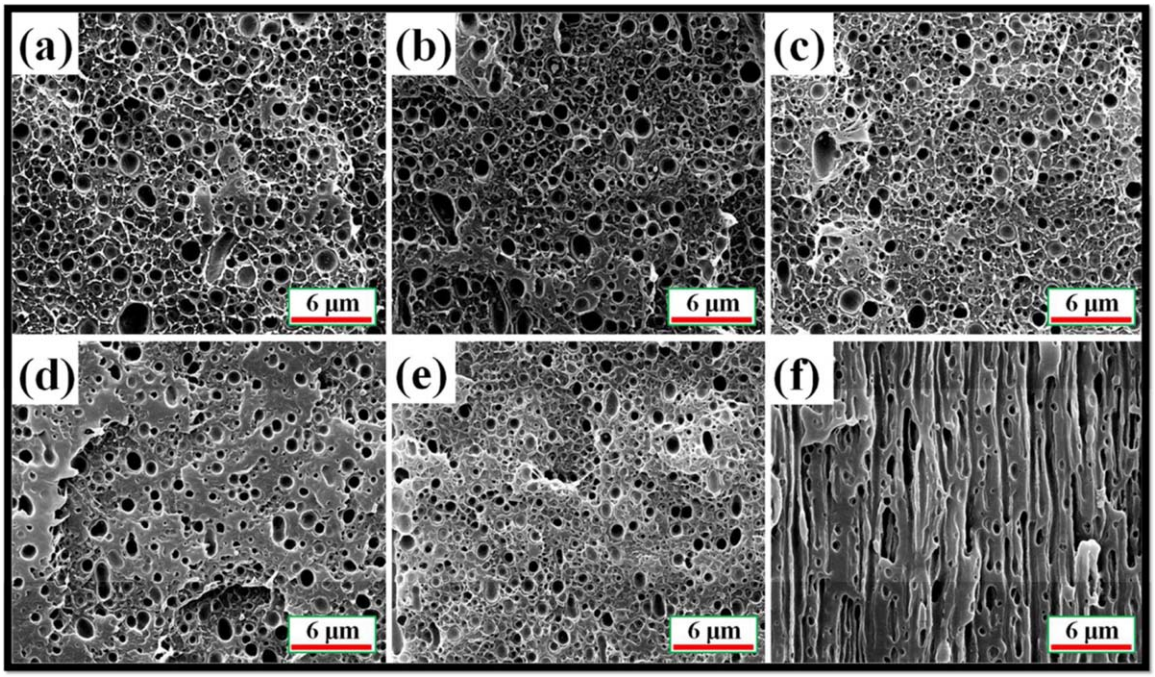

Figure 4. Morphology distribution of the short shot parts, the distance to the mold surface of (a)–(f) is 1450, 1400, 900, 220, 150, and 70 μm, respectively. [Color figure can be viewed in the online issue, which is available at wileyonlinelibrary.com.]

under intense flows.[32] According to Janssen's work, the deformation of dispersed phase and matrix phase in flow field will be closely to synchronization in case the viscosity ratio is about one.[33] It represents that the introduction of PS phase exerts little effect on the shear thinning behavior of the HDPE in such high shear rates. Therefore, the rheological behaviors of the HDPE/PS blend can roughly show the rheological behaviors of the neat HDPE under intense flows. As a result, due to the coordinated rheological behaviors of HDPE matrix and PS phase, the deformation of PS phase is harnessed to show the flow intensity in these conditions (injection molding, for example).

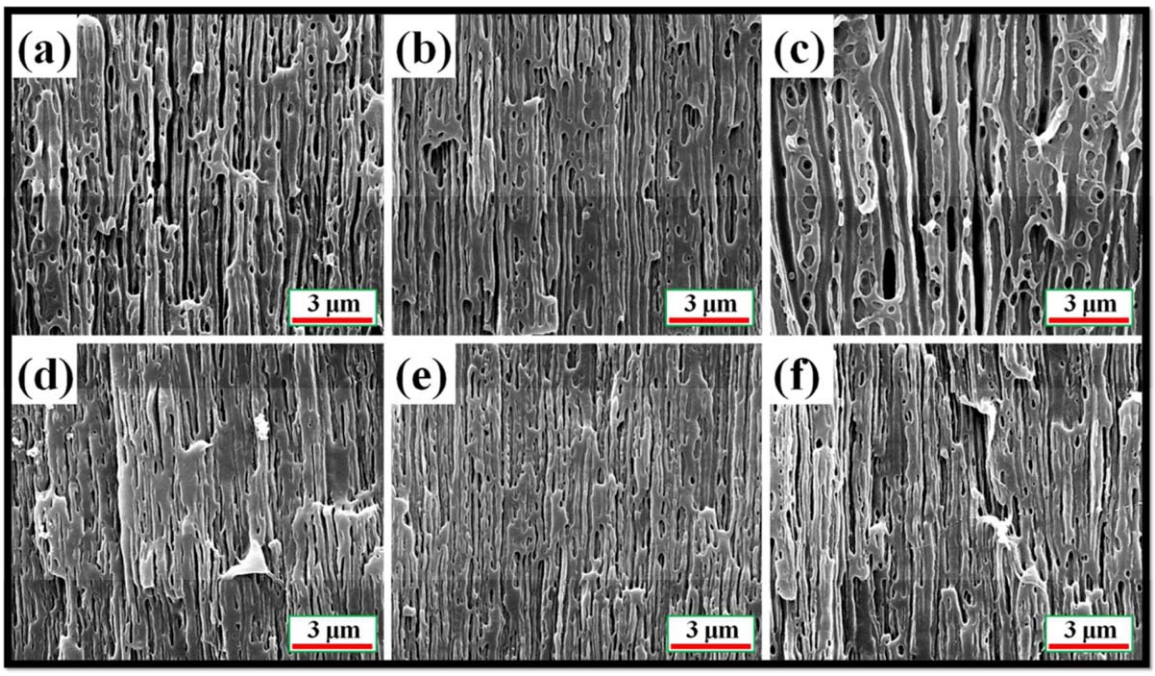

Figure 5. Morphology distribution of the GAIM parts under the gas penetration pressure with 10.4 MPa, the distance to the mold surface of (a)–(f) is 1450, 1400, 900, 220, 150, and 70 μm, respectively. [Color figure can be viewed in the online issue, which is available at wileyonlinelibrary.com.]

Table II. Diameters (μm) of the PS Phase in the Short Shot and GAIM Parts

Distance tomold surface (μm)	70	150	220	900	1350	1400	1450
SS parts	0.50 ± 0.10	0.58 ± 0.12	0.63 ± 0.15	0.78 ± 0.18	0.82 ± 0.18	0.84 ± 0.17	0.86 ± 0.19
6.2 MPa	0.21 ± 0.08	0.22 ± 0.07	0.19 ± 0.03	0.76 ± 0.25	0.27 ± 0.09	0.29 ± 0.08	0.33 ± 0.08
8.3 MPa	0.17 ± 0.06	0.18 ± 0.06	0.16 ± 0.02	0.67 ± 0.27	0.23 ± 0.08	0.26 ± 0.08	0.28 ± 0.08
10.4 MPa	0.13 ± 0.05	0.13 ± 0.04	0.12 ± 0.02	0.58 ± 0.31	0.20 ± 0.07	0.22 ± 0.08	0.24 ± 0.07

Phase Morphology in Short Shot Parts

The morphology in short shot parts is a typical skin-core structure. As shown in Figure 4, the dispersed phase is regularly distributed along the thickness direction. PS phase develops into fibrils in skin zone and the larger spherical droplets away from skin zone. It is widely accepted that the explanation of skin-core structure for common injection molding (CIM) parts is the theory of fountain flow.[32] Accordingly, without gas injection during short shot, the theory can also be used for the explanation of morphology distribution in the short shot parts. The PS droplets break up and become smaller with the results of elongational flow and biaxial stretching effect in melt front. Then, the PS fibrils or very fine sizes are formed in skin zone. Along with the increase in the distance from mold surface, the PS droplets with much larger diameters are formed because of both weaker flow field and higher temperature field.

Phase Morphology in the GAIM Parts

Due to additional second gas injection, GAIM parts display a particular hierarchical structure rather than a typical skin-core structure. As shown in Figure 5, the gas penetration pressure with 10.4 MPa plays an important role in the shape and distribution of the PS phase. In specific, as presented in Figure 5(a), the PS fibrils have been observed at gas channel zone, instead of large droplets reported in previous work.[28] The PS droplets experience from deformation to stretch, and develop into fibrils under the fierce flows.[34] More importantly, the additional gas cooling shortens the cooling stage of the melt, especially for the gas channel zone (Figure S1, Supporting Information). For the temperature-sensitive material under the rapid quenching,[35,36] the formed PS fibrils are instantly frozen, which can be deemed as the morphology after gas penetration. To further confirm the significance of gas cooling to the stability of PS phase, the smaller diameters of PS fibrils are measured at Figure 5(b) in comparison with at Figure 5(a), as listed in Table II. Nonetheless, as the position moves toward intermediate zone, the oriented PS phase is gradually slacked and replaced step by step by ellipsoidal and spherical droplets, as clearly shown in Figure 5(c). The PS phase in intermediate zone is deformed from droplets to fibrils when it subjects to strong flows. Unfortunately, the oriented PS phase is also exposed to high temperature field for long time, which causes oriented structures to gradually relax.[29–31] Clearly shown is the fact that the gas cooling exerts positive effects on the stability of PS fibrils in gas channel zone. When it comes to Figure 5(d,e)

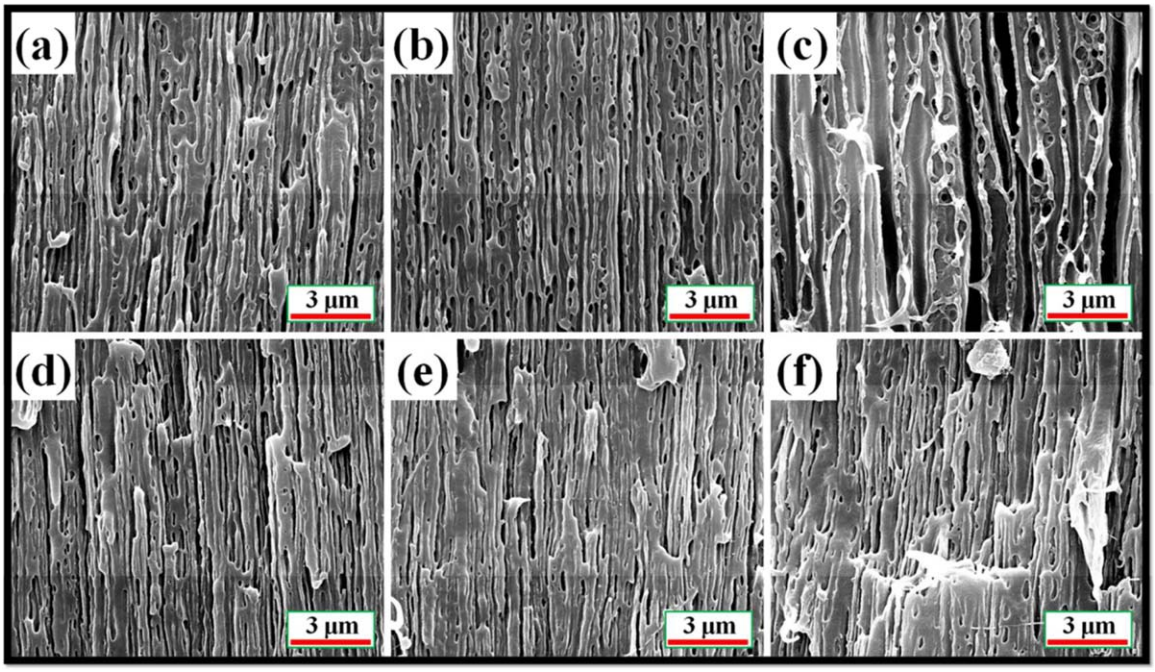

Figure 6. Morphology distribution of the GAIM parts under the gas penetration pressure with 8.3 MPa, the distance to the mold surface of (a)–(f) is 1450, 1400, 900, 220, 150, and 70 μm, respectively. [Color figure can be viewed in the online issue, which is available at wileyonlinelibrary.com.]

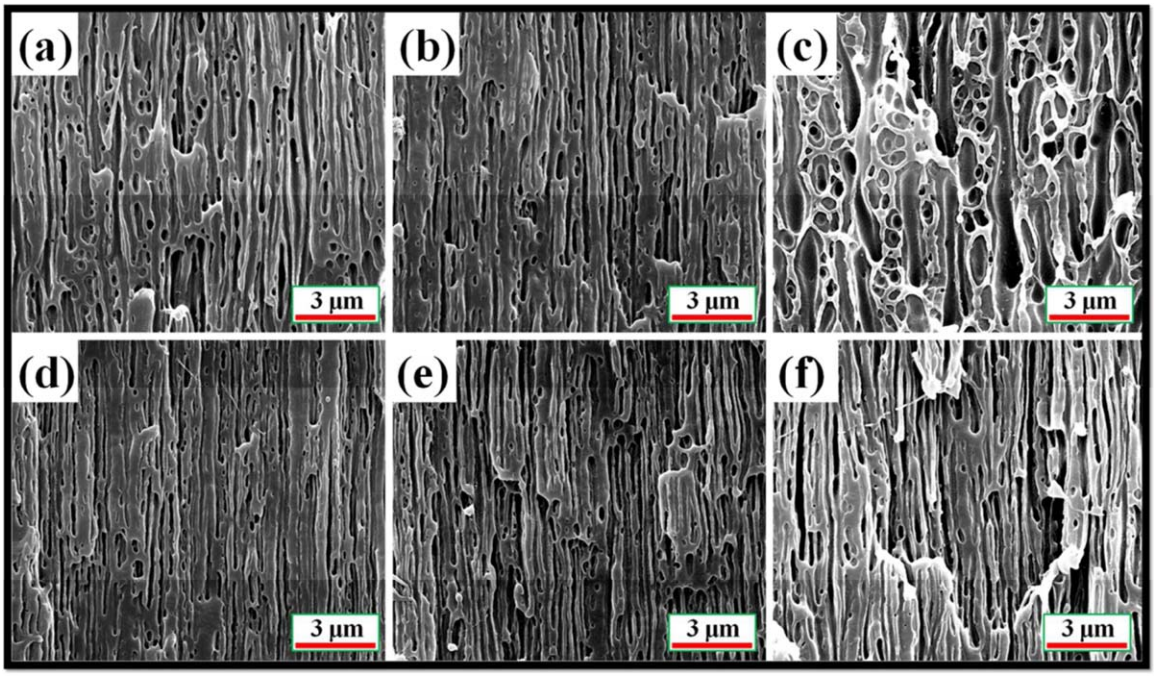

Figure 7. Morphology distribution of the GAIM parts under the gas penetration pressure with 6.2 MPa, the distance to the mold surface of (a)–(f) is 1450, 1400, 900, 220, 150, and 70 μm, respectively. [Color figure can be viewed in the online issue, which is available at wileyonlinelibrary.com.]

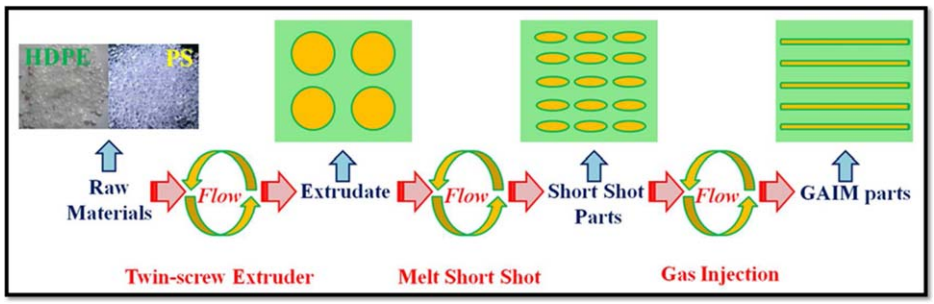

Figure 8. Morphological evolutions of PS phase in the blend from grains to fibrils. [Color figure can be viewed in the online issue, which is available at wileyonlinelibrary.com.]

representing subskin zone, the diameters of PS fibrils reach at the minimum values, as listed in Table II, which indicates the melt is exposed to intense flows. Meanwhile, since the heat conduction to mold wall is a major pathway to solidify polymer melt during molding process, this zone possesses much higher cooling rate due to much closer to the mold wall in comparison with intermediate zone. Accordingly, the relaxation behavior of PS phase in subskin zone is also negligible and can be regarded as the

Table III. Shear Strain (%) of the PS Phase by the Second Gas Penetration

Distance tomold surface (μm)	70	150	220	1350	1400	1450
6.2 MPa	196	226	301	271	255	222
8.3 MPa	260	291	368	328	292	275
10.4 MPa	359	424	506	386	356	330

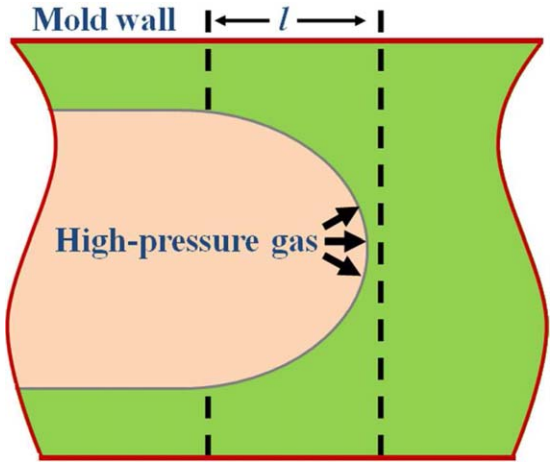

Figure 9. Diagram of the gas front during the second gas penetration stage. [Color figure can be viewed in the online issue, which is available at wileyonlinelibrary.com.]

Table IV. Key Parameters of the Second Gas Penetration

Gas pressure	l (mm)	t_p (s)	t_s (s)
6.2 MPa	1.02	0.82	0.0046
8.3 MPa	1.24	0.68	0.0047
10.4 MPa	1.62	0.58	0.0052

morphology after gas penetration. Finally, the orientation degree of PS phase slightly decreases in Figure 5(f) representing skin zone. Due to the highest cooling rate in this zone near to the mold wall, the polymer melt comes near to the end of solidification stage and then has relatively high viscosity during gas penetration stage. Therefore, gas penetration effects in skin zone are slighter than that of in subskin zone on the formation of final morphology.

Gas penetration pressure is found to be an effective factor contributing to the shape and distribution of the PS phase in the HDPE matrix. Figures 6 and 7 depict the gas penetration pressures of 8.3 and 6.2 MPa on the phase morphology, respectively. The variation trends of the sizes of PS phase along the parts thickness are analogous to the parts with 10.4 MPa, displaying as "*W*" shape. Nonetheless, all the diameters of PS phase in relevant zone are increased with the decreasing gas penetration pressure, as listed in Table II. The difference of phase morphology indicates the intensity of second flow field closely depends on the gas penetration pressure.

Morphological Evolution of PS Phase

Figure 8 depicts the diagram of the PS phase suffered from successive flows. The first flow is the melting blend for HDPE/PS. The raw PS particles are changed into large PS droplets under a twin-screw extruder (Figure S2, Supporting Information). The second flow is the melt short shot. The large PS droplets are broken into smaller droplets and ellipsoids under intense flows and high temperature field, as shown in Figure 4. The third flow is triggered by the second gas penetrating the first melt. The smaller PS droplets and ellipsoids are exposed again to fierce flows and stretched into PS fibrils,[28] as shown in Figures 5–7. Clearly shown is that the GAIM possesses complex flow fields concerning multiphase multiflows. It should be pointed out again that our main goal is to describe the second flow field triggered by the second gas penetrating the first melt. Therefore, the PS sizes in both short shot parts and GAIM parts only need to be considered when calculates shear rate with the classical models for predicting the shapes of dispersed phase in immiscible blend.

Table V. Shear Rate (s^{-1}) in the Cavity during the Second Gas Penetration Stage

Distance tomold surface (μm)	70	150	220	1350	1400	1450
6.2 MPa	426	491	654	589	554	483
8.3 MPa	553	619	783	698	621	585
10.4 MPa	690	815	973	742	685	635

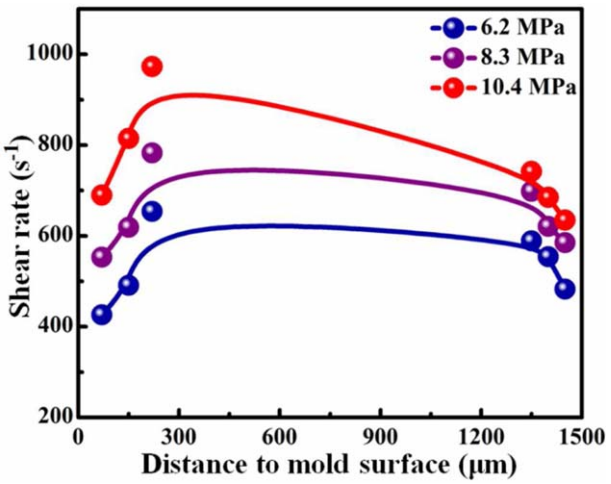

Figure 10. Shear fields with various second gas penetration pressures. [Color figure can be viewed in the online issue, which is available at wileyonlinelibrary.com.]

Applied Total Strain

Table II provides the diameters of PS droplets or fibrils in both short shot parts and GAIM parts based on the SEM observation. The relaxation of oriented structures in gas channel zone has been successfully controlled by the incorporation of gas cooling. At the same time, the oriented PS phase in subskin and skin zone is also perfectly retarded by the main way of heat conduction to the mold wall. Besides, due to much larger relaxation, the diameters of PS phase in intermediate zone are unable to show the real imposed strain and then should be abandoned. Therefore, the available deformation of PS phase in GAIM parts based on short shot parts is utilized to show the second flow field.

The complex flow fields in an injection molding composed of shear stress along with velocity gradient and elongational flow and biaxial stretching effect in melt front are generated simultaneously and give rise to polymer morphological evolutions. Accordingly, the complex flow fields are also produced by the second gas penetrating and advancing the first melt. For an accurate but simple calculation, the shear flow is overall assumed as the equal effects of the complex flow fields on the morphological evolution. Thereby, a characteristic shear rate ($\dot{\gamma}$) is defined, which can be reversely calculated with the classical models for predicting the shapes of dispersed phase in immiscible blend.

The shear strain (γ) of PS phase caused by the second gas penetrating the first melt can be quantitatively calculated. For the second flow field, the previous work reveals the values of C_a are considerably high,[27–31] meanwhile, the difference in viscosity between the selected HDPE and PS is negligible under intense flows, as shown in Figure 3. Therefore, the deformation of PS droplets can be considered as an "affine" droplet deformation during gas penetration.[21,24] In addition, almost all PS droplets have been transformed into PS fibrils with various diameters. Hence, the Eqs. (2) and (3) representing the ellipsoidal model can be reasonably employed to reversely calculate the imposed strains.[21] Combined with Table II and the equations, the shear

strains with various gas penetration pressures are evaluated, as listed in Table III.

Flow Duration

The gas penetration behavior in the cavity should be seriously considered in order to further obtain the quantitative intensity of second flow field. A fierce flow is created when gas penetrating melt and the gas cooling stage is absence of flow on melt in that the zone near to the gas channel is definitely frozen by gas rapid quenching (Fig. S1, Supporting Information). Namely, the flow field is generated with gas penetrating melt. What is more, the flow field mainly distributes at the region around gas front.[37] So the length of gas front, l, is roughly regarded as the region with the interaction of flow, as shown in Figure 9. Controlled appropriate gas penetration time (0.40 s, in this work), the main cavity is not occupied entirely, resulting in a cone shape of gas front in the unfinished parts. Then, the values of l can be measured by Vernier caliper, which are enhanced with the increasing gas pressures, as listed in Table IV. Besides, two pressure sensors are mounted on the gas inlet and at the end of main cavity, respectively. Therefore, the gas penetration time (t_p, Table IV) can be exactly determined when the gas discharges outside, which is to better reflect the real molding process rather than the values with unknown accuracy from the simulation.[28,38] Then the average flow duration (t_s) can be gained according to the equal average melt advancing velocity along the flow direction, as listed in Table IV. Consequently, the average flow duration is gradually increased with the increasing gas penetration pressure.

Description of the Flow Field

Combined with the above results, the values of shear rate are safely calculated with eq. (4), as provided in Table V. Due to the accurate parameters from measurement and observation, the results are more dependable than the previous simulation results.[28,38] Accordingly, based on the calculated values of shear rate in the relevant zones as well as the nature of continuous distribution of flow field under molding conditions, the desired distribution of shear rates along the whole thickness are successfully obtained even if it lacks the values of intermediate zone, as clearly depicted in Figure 10. It represents that the subskin zone has the highest shear rate, whereas the gas channel zone has the lowest shear rate. Furthermore, the shear rates are enhanced with the increasing gas pressures. These results are good interpretations of the formation of hierarchical structures for polymers in the second flow field.[16,17,28–31] More importantly, the gas penetration time (t_p) is inversely proportional to the shear intensity, as shown in the relation (4), which can be used as a basis for the qualitative comparison of the intensity for the complex flow fields with various conditions. Beyond that the second flow field can be designed by tailoring penetration power (such as gas, water, melt injection pressure) as well as penetration resistance along with melt viscosity (such as temperature gradient, polymer molecular parameters),[39] which contributes to realizing the optimum coupling between external fields (such as stress and temperature) and chain architectures, and then elastically tunes the morphologies and physical properties of polymers.

$$\dot{\gamma} \propto \frac{1}{t_p}, \tag{4}$$

CONCLUSIONS

In this study, since the relaxation behaviors of the PS phase in the HDPE matrix are successfully retarded by incorporation of additional gas cooling, the second flow field triggered by gas penetrating melt is quantitatively described with the classical models for predicting the shapes of dispersed droplets in immiscible blend. The higher gas penetration pressures lead to the stronger flow intensity while result in the shorter gas penetration time. The gas penetration time can be used as a basis for the qualitative comparison of the flow fields under various conditions. More importantly, the second flow field can be tailored by changing melt advancing rate, such as the penetration power, the penetration resistance, which contributes to realizing the optimum coupling between complex external fields and chain architectures and designing polymer products with desired hierarchical structures and performance. Besides, this work breaks a new path for the exploration of real flow field in various processing conditions.

ACKNOWLEDGMENTS

We express our sincere thanks to the National Natural Science Foundation of China (NNSFC, Grant Nos. 21174092, 51421061) and the Platform Foundation of State Key Laboratory Cultivation Base for Nonmetal Composites and Functional Materials (Grant Nos. 14tdfk04, 14zx7170) for financial support.

REFERENCES

1. Wang, K.; Chen, F.; Li, Z.; Fu, Q. *Prog. Polym. Sci.* **2014**, *39*, 891.
2. Buchma, M.; Theriault, R.; Osswald, T. A. *Polym. Eng. Sci.* **1997**, *37*, 667.
3. Chang, R. Y.; Yang, W. H. *Int. J. Numer. Meth. Fluids* **2001**, *37*, 125.
4. Bress, T. J.; Dowling, D. R. *Polym. Eng. Sci.* **2013**, *53*, 770.
5. Nagel, J.; Heinrich, G. *Int. J. Heat Mass Transfer* **2012**, *55*, 6890.
6. Luo, Y. M.; Chevalier, L.; Utheza, F.; Monteiro, E. *Polym. Eng. Sci.* **2013**, *53*, 2683.
7. Liu, J.; Tai, H.; Howdle, S. M. *Polymer* **2005**, *46*, 1467.
8. Poncet, S.; Boiteux, G.; Pascault, J. P.; Sautereau, H.; Seytre, G.; Rogozinski, J.; Kranbuehl, D. *Polymer* **1999**, *40*, 6811.
9. Chvátalová, L.; Navrátilová, J.; Cermák, R.; Raab, M.; Obadal, M. *Macromolecules* **2009**, *42*, 7413.
10. Janeschitz-Kriegl, H.; Ratajski, E. *Polymer* **2005**, *46*, 3856.
11. Janeschitz-Kriegl, H. *Colloid Polym. Sci.* **2003**, *281*, 1157.
12. Lamberti, G. *Chem. Soc. Rev.* **2014**, *43*, 2240.
13. Gurvara-Morales, A.; Figueroa-López, U. *J. Mater. Sci.* **2014**, *49*, 4399.
14. Murase, H.; Ohta, Y.; Hashimoto, T. *Polymer* **2009**, *50*, 4727.

15. Hosseini, A. M.; Chotenovsky, D.; Farrell, K.; Farrell, S. A.; Sparrey, C. J. *Polym. Test.* **2014**, *38*, 1.
16. Zheng, G. Q.; Huang, L.; Yang, W.; Yang, B.; Yang, M. B.; Li, Q.; Shen, C. Y. *Polymer* **2007**, *48*, 5486.
17. Liu, X.; Zhang, C.; Dai, K.; Zheng, G.; Liu, C.; Shen, C. *Polym. Adv. Technol.* **2013**, *24*, 270.
18. Huang, H. X.; Wang, B.; Zhou, W. W. *Compos. B* **2012**, *43*, 972.
19. Akay, G. *Polym. Compos.* **1983**, *4*, 256.
20. Zhang, K.; Liu, Z.; Yang, B.; Yang, W.; Lu, Y.; Wang, L.; Sun, N.; Yang, M. *Polymer* **2011**, *52*, 3871.
21. Jansseune, T.; Vinckier, I.; Moldenaers, P.; Mewis, J. *J. Non-Newtonian Fluid Mech.* **2001**, *99*, 167.
22. Vananroye, A.; van Puyvelde, P.; Moldenaers, P. *Langmuir* **2006**, *22*, 2273.
23. Yamane, H.; Takahashi, M.; Hayashi, R.; Okamoto, K.; Kashihara, H.; Masuda, T. *J. Rheol.* **1998**, *42*, 567.
24. Elemans, P. H. M.; Bos, H. L.; Janssen, J. M. H.; Meijer, H. E. H. *Chem. Eng. Sci.* **1993**, *48*, 267.
25. Almusallam, A. S.; Larson, R. G.; Solomon, M. J. *J. Rheol.* **2000**, *44*, 1055.
26. Yu, W.; Bousmina, M. *J. Rheol.* **2003**, *47*, 1011.
27. Wang, L.; Yang, M. B.; Zhang, Q. P.; Zhang, R. Y.; Wu, J. J.; Feng, J. M. *Polym. Adv. Technol.* **2013**, *24*, 541.
28. Zheng, G. Q.; Yang, W.; Huang, L.; Li, Z. M.; Yang, M. B.; Yin, B.; Li, Q.; Liu, C. T.; Shen, C. Y. *J. Mater. Sci.* **2007**, *42*, 7275.
29. Xia, X. C.; Zhang, Q. P.; Wang, L.; Feng, J. M.; Yang, M. B. *Macromol. Chem. Phys.* **2014**, *215*, 1146.
30. Zhang, Q. P.; Wang, L.; Xia, X. C.; Fu, X. R.; Feng, J. M.; Yang, M. B. *J. Appl. Polym. Sci.* **2014**, *131*, 40349.
31. Xia, X. C.; Zhang, Q. P.; Wang, L.; He, S.; Feng, J. M.; Yang, M. B. *Polym. Int.* **2014**, *63*, 1997.
32. Fellahi, S.; Favis, B.; Fisa, B. *Polymer* **1996**, *37*, 2615.
33. Janssen, P. J. A.; Vananroye, A.; van Puyvelde, P.; Moldenaers, P.; Anderson, P. D. *J. Rheol.* **2010**, *54*, 1047.
34. Mikami, T.; Cox, R. G.; Mason, S. G. *Int. J. Multiphase Flow* **1975**, *2*, 113.
35. Saron, C.; Felisberti, M. I. *Mater. Sci. Eng: A* **2004**, *370*, 293.
36. Dutt, G.; Kit, K. M. *J. Appl. Polym. Sci.* **2003**, *87*, 1975.
37. Gauri, V.; Koelling, K. W. *J. Non-Newtonian Fluid Mech.* **1999**, *83*, 183.
38. Hu, S.; Yang, W.; Liang, S. P.; Yang, B.; Yang, M. B. *J. Macromol. Sci. B: Phys.* **2009**, *48*, 1084.
39. Zhang, Q. P.; Xia, X. C.; He, S.; Feng, J. M.; Yang, M. B.; Li, Y. T.; Zhou, Y. L. *Macromol. Mater. Eng.* **2015**, *300*, 901.